1 **Highly Heterogeneous Depleted Mantle Recorded in the Lower Oceanic Crust**

2 Sarah Lambart[1,2]*, Janne M. Koornneef[3], Marc-Alban Millet[1], Gareth R. Davies[3], Matthew Cook[1],

3 C. Johan Lissenberg[1]

4

5 [1.] Cardiff university, School of Earth and Ocean Sciences, Cardiff, United Kingdom

6 [2.] University of Utah, Department of Geology and Geophysics, Salt Lake City, United States

7 [3.] Vrije Universiteit Amsterdam, Faculty of Science, Amsterdam, The Netherlands

8

9 **The Earth's mantle is heterogeneous as a result of early planetary differentiation and**

10 **subsequent crustal recycling during plate tectonics. Radiogenic isotope signatures of mid-**

11 **ocean ridge basalts have been used for decades to map mantle composition, defining the**

12 **depleted mantle end member. These lavas, however, homogenize via magma mixing and may**

13 **not capture the full chemical variability of their mantle source. Here we show that the**

14 **depleted mantle is significantly more heterogeneous than previously inferred from the**

15 **compositions of lavas at the surface, extending to highly enriched compositions. We perform**

16 **high spatial resolution isotopic analyses on clinopyroxene and plagioclase from lower crustal**

17 **gabbros drilled on a depleted ridge segment of the northern Mid-Atlantic Ridge. These**

18 **primitive cumulate minerals record nearly the full heterogeneity observed along the northern**

19 **Mid-Atlantic Ridge, including hotspots. Our results demonstrate that substantial mantle**

20 **heterogeneity is concealed in the lower oceanic crust and that melts derived from distinct**

21 **mantle components can be delivered to the lower crust on a centimetre scale. These findings**

22 **provide a starting point for re-evaluation of models of plate recycling, mantle convection, and**

23 **melt transport in the mantle and the crust.**

24 The mantle, Earth's largest geochemical reservoir and main source of volcanism, records the time-

25 integrated history of recycling of oceanic lithosphere and its overlying sediments during the plate

26 tectonic cycle[1,2]. The compositional heterogeneity thus generated within the mantle reflects this

27   recycling process[2,3]; determining the magnitude and length scale of this heterogeneity will enable a

28   reconstruction of the recycling process and mantle convection, ultimately providing a window onto

29   the dynamics of our planet. Mid-ocean ridge basalts (MORB) have been the primary tool to map

30   geochemical heterogeneity of the oceanic upper mantle for decades[3-5]. However, because MORB

31   mix in crustal magma chambers[6,7], the degree to which they are representative of its mantle source

32   remains poorly constrained. Hence, the true heterogeneity of the MORB mantle source is uncertain,

33   providing a significant barrier to understanding the magnitude and scale of recycled crust and the

34   long-term evolution of the mantle.

35   One approach is to analyse the isotopic compositions of abyssal peridotites. These mantle samples

36   may preserve a wider range of isotopic compositions than associated lavas[7-14]. However, they

37   represent the melting residue of the MORB source, and potentially could have therefore lost the

38   most fusible material[10] (pyroxenite, eclogite) thought to represent recycled, enriched, components[1].

39   Furthermore, interpretations are complicated by the common occurrence of recent refertilization in

40   the lithospheric mantle beneath the ridge axis[11-13] and severity of alteration[7,11].

41   In this study, we overcome this problem by conducting crystal-scale Nd and Sr isotopic analyses on

42   primitive cumulate minerals from the lower oceanic crust, and show that these cumulate minerals

43   crystallised from heterogeneous melts extending to significantly more enriched compositions, than

44   the associated MORB.

45

46   **High magnitude small-scale heterogeneity in cumulate minerals**

47   This study focuses on the Mid-Atlantic Ridge (MAR) segment north of the Atlantis Transform

48   Fault (30°N), which is predominantly composed of volcanic rocks with isotopically depleted,

49   normal mid-ocean ridge basalt (N-MORB) compositions[15]. Along the ridge-transform intersection,

50   an uplifted dome of ultramafic and mafic plutonic rocks exposed by detachment faulting (the

51   Atlantis Massif[16]) provides a window into the lower oceanic crust. Drill core of gabbroic cumulates

52   (International Ocean Drilling Program, IODP Hole U1309D) yielded a detailed, 1415 m record of

53 the lower crust[16], which, along with the associated volcanic rocks, provides a unique opportunity to

54 compare the isotopic heterogeneity of melts delivered to the lower crust with those erupted onto the

55 seafloor. Results of Nd (^{143}Nd/^{144}Nd) and Sr (^{87}Sr/^{86}Sr) isotopic analyses on individual micro-

56 drilled clinopyroxene and plagioclase crystal domains from plutonic rocks of Hole U1309D are

57 shown in Fig. 1. We compare these data with whole rock isotopic compositions of diabase and

58 microgabbros collected on the same core, associated basalts flows (IODP Sites U1310 and U1311),

59 and Atlantic MORB and abyssal peridotite data from the literature, in Figs 1 and 2.

60   The results indicate that cumulate minerals: (1) are significantly more isotopically

61 heterogeneous than the associated diabase and lavas, exceeding the range of ^{143}Nd/^{144}Nd in MORB

62 from 30°N by a factor of seven (Fig. 1); (2) capture a significant proportion of mantle heterogeneity

63 reported in abyssal peridotites (Fig. 2a,b); and (3) record almost the full Nd isotopic heterogeneity

64 currently observed in all of North Atlantic MORB (including the enriched, plume-influenced

65 Azores platform, Iceland and Jan Mayen; Fig. 2a,b). Furthermore, Nd isotopic heterogeneity occurs

66 down to the centimetre scale, with plagioclase and clinopyroxene from individual samples

67 commonly not in isotopic equilibrium (Fig. 3). This small-scale heterogeneity can be explained by

68 multiple replenishments in the crystal mush leading to dissolution-crystallization episodes[17] and

69 juxtaposition of diverse populations of crystals[18]. At the grain scale, cores show more primitive

70 compositions (higher Mg# in clinopyroxene and anorthite content in plagioclase) than rims (see

71 Supplementary Fig. 1) suggesting that the cores crystallized from primitive melts upon melt

72 emplacement in the crust, while rims crystallized from late-stage percolating melts[19]. Once minerals

73 have formed, Nd diffusion is too slow to destroy grain-scale heterogeneity: at the solidus

74 temperature of a gabbro Nd zoning is preserved in calcic plagioclase on a 100μm-scale for more

75 than 10Myrs[20]; diffusion of Nd in clinopyroxene is even slower[21].

76   ^{87}Sr/^{86}Sr ratios are similarly variable. Most plagioclase data fall on the Sr-Nd isotopic data

77 array defined by global MORB (Supplementary Fig. 2) and could conceivably represent primary

78 values. However, clinopyroxenes typically record higher ^{87}Sr/^{86}Sr than plagioclase, suggesting

79   seawater alteration may have overprinted mantle signatures. Hence, we use only Nd isotope data for

80   the interpretation.

81   A t-test shows no statistical difference between clinopyroxene and plagioclase ^{143}Nd/^{144}Nd but

82   together, the cumulate minerals represent a distinct population compared to basalt, diabase and

83   microgabbros (*p*-value <0.0002). However, the mean whole rock ^{143}Nd/^{144}Nd of the diabase,

84   microgabbros, and associated basalt flows (0.513198±41) is within the 2σ error of that of the

85   cumulate minerals (0.513138±187). Thus, there is no difference in the average compositions of the

86   cumulate minerals relative to the basalt, diabase and microgabbros, but cumulate minerals record a

87   larger variability. This indicates that cumulate minerals represent products of crystallization of

88   small amount of melts that have undergone limited mixing before being delivered to the crust,

89   whereas erupted MORB represent averages of much higher volumes of magmas that have been

90   significantly mixed together at shallower depths.

91

92   **Depleted mantle composition and temperature variations**

93   These findings have important implications for both the magnitude and scale of heterogeneity

94   of the upper mantle. The striking similarity of the Nd isotopic frequency distribution of cumulate

95   minerals at Hole U1309D with that of North Atlantic MORB as a whole (Fig. 4) indicates that

96   mantle heterogeneity beneath the Atlantis Massif is representative of the magnitude of

97   heterogeneity in the North Atlantic basin. It follows that it is the proportion of recycled material in

98   the aggregated magma, rather than the degree of isotopic enrichment of the recycled material in

99   the source, that is responsible for variations in MORB isotopic compositions. If so, along-axis

100   MORB variations should record the proportion of each component in MORB and in the mantle

101   source along the axis. To assess this hypothesis, we use an adiabatic mantle melting model[22] to

102   calculate: (i) the required proportion of recycled, material-derived melt to reproduce the Nd isotopic

103   ratio of North Atlantic MORB (see Methods); (ii) the corresponding fraction of recycled material in

104   the mantle source; and (iii) the thickness of oceanic crust generated along the ridge axis. It has been

105   suggested that MORB at the scale of a ridge segment (i.e., ~ 300 km) experienced common

106   differentiation processes[23]. Hence, we used the weighted average MORB compositions at a segment

107   scale. The melt derived from the recycled material has a higher Nd abundance than depleted

108   peridotitic melt[11]. Hence, adding a small amount of depleted peridotitic melt to the recycled

109   material-derived melt does not significantly affect the isotopic composition of the latter.

110   Conversely, even a small contribution of recycled material-derived melt can significantly modify

111   the isotopic composition of the depleted peridotite melt in such a way that the isotopic signature of

112   the depleted component is unlikely to be preserved in the cumulate minerals (see Methods). Hence,

113   we used the most enriched composition recorded in cumulates ($^{143}/^{144}$Nd = 0.512800±15) and the

114   most depleted composition recorded in North Atlantic abyssal peridotites ($^{143}/^{144}$Nd =

115   0.513662±18)[7] as isotopic compositions of the mantle end-members. Assuming the recycled

116   material is represented by recycled oceanic crust[24] (see Methods), the calculation yields a

117   proportion of recycled material-derived melt in locally averaged MORB of 27-59% (Fig. 2c). This

118   proportion is a function of both the proportion of recycled material in the source and the mantle

119   potential temperature (Supplementary Fig. 6a). To convert the proportion of recycled material-

120   derived melt in MORB to a proportion of recycled material in the mantle we performed three sets of

121   calculations: (1) we fixed the mantle potential temperature to T_P = 1300°C and calculated the

122   fraction of recycled material in the source required to explain the melt compositions; (2) we fixed

123   the fraction of recycled material in the mantle at 4% (i.e., the average fraction estimated in the first

124   set of calculations) and calculated the T_P required to explain the melt compositions; and (3) in a

125   hybrid model, we varied both the proportion of recycled material and the mantle potential

126   temperature. These calculations also yield melt volume, and hence crustal thickness. To evaluate

127   the validity of these models we compare the calculated crustal thickness for each ridge segment

128   with their average seafloor depth, a proxy for crustal thickness[25] (Fig. 2d and Supplementary Fig.

129   6b-e).

130   Varying the mantle potential temperature alone clearly failed to match the elevation profile by

131   creating negative thickness anomalies around the major hot spots and producing crustal thickness

132   variations much larger than those observed in the Atlantic basin[26]. Furthermore, it required a large

133   range of mantle potential temperatures (1180-1440°C). It is worth noting, however, that varying the

134   potential temperature of a heterogeneous mantle can create a negative correlation between the

135   contribution of the pyroxenite in the melt (Fig. 2c) and the crustal thickness (Supplementary Fig.

136   6b), as observed for the Vema lithospheric section[12]. Varying the proportion of recycled material

137   alone did not reproduce small scale elevation variations on ridge segments far from the hot spots[27].

138   It also did not reproduce the bathymetry anomaly centered on Iceland. This anomaly is attributed to

139   a significantly thickened crust (> 10 km)[26], likely produced by higher mantle potential temperature

140   or high melt flux[28]. However, large-scale variations, such as the higher elevations of Jan Mayen and

141   the Azores platform, are overall better correlated with thickness variations due to small variations of

142   proportions of recycled material in the source rather than with thickness variations due to

143   temperature variations. The best match is obtained by the hybrid model. Considering a variation of

144   crustal thickness between 3 and 11 km[26], both compositional and elevation profiles are reproduced

145   by varying T_P between 1245°C and 1367°C and the proportion of recycled material in the source

146   between 3.2 and 8.5% (Fig. 2d; Supplementary Fig. 6d-e). Hence, our calculations support a model

147   where higher proportion of recycled material in the source around the hot spot creates clear crustal

148   thickness and chemical anomalies along most of the northern MAR without requiring large

149   (>120°C) thermal variations.

150

151   **Limited magma mixing during melt transport in the mantle**

152   The finding of high-magnitude mantle heterogeneity delivered to the crust down to the

153   centimetre scale requires that the MORB source is heterogeneous on a length scale smaller than the

154   melting region. Variations of melt production have been observed along the northern MAR on a

155   scale of 25-50 km[29]. If this length scale of variation is due to various proportions of mantle

156   components in the source region, then the scale of individual compositional domains must be

157   smaller. Short (10^{-3} to 10^{-2} m) Nd (and Sr) isotopic heterogeneity can persist over timescales of 10^9

158   yr in the solid mantle[30]. However, short mantle heterogeneities decrease the likelihood of extracting

159   the melt in (chemical) isolation, and melt-solid diffusion may destroy the isotopic signatures.

160   Hence, our study supports the prevalence of a kilometer size length scale of heterogeneity in the

161   MORB mantle source[12,31].

162   Crucially, the isotopic heterogeneity we observe in the Atlantis Massif cumulate minerals

163   provides strong evidence that heterogeneous melts are delivered to the lower crust without

164   significant mixing. Most melt generated by decompression melting is considered to be extracted

165   from the mantle through high-permeability channels[32,33]. It has previously been argued that

166   channelised melt transport is accompanied by significant mixing[31]. However, if this were the case, it

167   would quickly dilute heterogeneous isotopic compositions. Hence, our results suggest that magma

168   mixing inside the channels is limited. We propose that each mantle component could generate its

169   own network of channels to account for both preservation of isotopic heterogeneities and rapid

170   magma transport[34] (Fig. 5). Melt-rock reactions between recycled material-derived melt and

171   subsolidus peridotite favour a (near) closed-system evolution[35,36], and thermal diffusion can

172   nucleate channelization that preferentially samples melts from the most fusible component[37,38].

173   Eventually, magmas from the less fusible adjacent mantle can also start to focus together through

174   reactive or mechanical instabilities[30,33]. Such processes would discourage mixing between magmas

175   derived from each component and preserve extreme isotopic compositions (Fig. 5).

176   In conclusion, the isotopic heterogeneity revealed in the lower oceanic crust provides strong

177   evidence that the limited isotopic variability recorded in MORB is a consequence of crustal-level

178   mixing of melts form a highly heterogeneous source. Furthermore, our novel analytical approach

179   offers considerable potential to assess the full heterogeneity delivered to the crust across a range of

180   geodynamics settings. Finally, these new findings require re-evaluations of models for convective

181   thinning and stretching during mantle convection[39,40] and for melt migration through the mantle and

182   the crust[31,41] to account for greater isotopic heterogeneity and limited magma mixing in the depleted

183   mantle.

184

185   **References**

186   1. Allègre, C.J., Turcotte, D.L. Implications of a two-component marble-cake mantle. *Nature* 323,

187   123-127 (1986).

188   2. Hofmann, A. W. Mantle geochemistry: the message from oceanic volcanism. *Nature* 385, 219–

189   229 (1997).

190   3. Hart, S. R. Heterogeneous mantle domains: signatures, genesis and mixing chronologies. *Earth*

191   *Planet. Sci. Lett.* 90, 273–296 (1988).

192   4. White, W. M. Sources of oceanic basalts: Radiogenic isotopic evidence. *Geology* 13(2), 115-

193   118 (1985).

194   5. Cohen, R. S., Evensen, N. M., Hamilton, P. J., O'Nions, R. K. U–Pb, Sm–Nd and Rb–Sr

195   systematics of mid-ocean ridge basalt glasses. *Nature* 283, 149-153 (1980).

196   6. Batiza, R. Inverse relationship between Sr isotope diversity and rate of oceanic volcanism has

197   implications for mantle heterogeneity. *Nature* 309, 440-441 (1984).

198   7. Cipriani, A., Brueckner, H. K., Bonatti, E., Brunelli, D. Oceanic crust generated by elusive

199   parents: Sr and Nd isotopes in basalt-peridotite pairs from the Mid-Atlantic Ridge. *Geology* 32,

200   657-660 (2004).

201   8. Stracke, A. et al. Abyssal peridotite Hf isotopes identify extreme mantle depletion. *Earth*

202   *Planet. Sci. Lett.* 308, 359-368 (2011).

203   9. Warren, J. M. Global variations in abyssal peridotite compositions. *Lithos* 248, 193-219 (2016).

204   10. Salters, V.J.M., Dick, H.J.B. Mineralogy of the mid-ocean-ridge basalt source from neodymium

205   isotopic composition of abyssal peridotites. *Nature* 418, 68-72 (2002).

206   11. Warren, J. M., Shimizum N., Sakaguchi, C., Dick, H. J. B., Nakamura, E. An assessment of

207   upper mantle heterogeneity based on abyssal peridotite isotopic compositions. *J. Geophys. Res.*

208   *Solid Earth* 114, B12203 (2009).

209   12. Brunelli, D., Cipriani, A., Bonatti, E. Thermal effects of pyroxenites on mantle melting below

210   mid-ocean ridges. *Nature Geosci.* 11, 520-525 (2018).

211   13. Mallick, S., Dick, H. J., Sachi-Kocher, A., Salters, V. J. Isotope and trace element insights into

212   heterogeneity of subridge mantle. *Geochem. Geophys. Geosyst.* 15(6), 2438-2453 (2014).

213   14. Snow, J. E., Hart, S.R., Dick H.J.B. Nd and Sr isotope evidence linking mid-ocean-ridge basalts

214   and abyssal peridotites. *Nature* 371, 57-60 (1994).

215   15. Gale, A., Dalton, C. A., Langmuir, C. H., Su, Y., Schilling, J. G. The mean composition of

216   ocean ridge basalts. *Geochem. Geophys. Geosyst.* 14(3), 489–518 (2013).

217   16. Blackman, D. K. et al. Drilling constraints on lithospheric accretion and evolution at Atlantis

218   Massif, Mid   Atlantic Ridge 30°N. *J. Geophys. Res.* 116, B07103 (2011).

219   17. Leuthold, J., Lissenberg, C. J., O'Driscoll, B., Karakas, O., Falloon, T., Klimentyeva, D. N.,

220   Ulmer, P. Partial melting of lower oceanic crust gabbro: constraints from poikilitic

221   clinopyroxene primocrysts. *Frontiers in Earth Sci.* 6, 15 (2018).

222   18. Schleicher, J. M., Bergantz, G. W. The mechanics and temporal evolution of an open-system

223   magmatic intrusion into a crystal-rich magma. *J. Petrol.* 58(6), 1059-1072 (2017).

224   19. Lissenberg, C. J., MacLeod, C. J. A reactive porous flow control on mid-ocean ridge magmatic

225   evolution. *J. Petrol.* 57(11-12), 2195-2220 (2016).

226   20. Cherniak, D. J. REE diffusion in feldspar. *Chem. Geol.* 193(1-2), 25-41 (2003).

227   21. Van Orman, J. A., Grove, T. L., Shimizu, N. Rare earth element diffusion in diopside: influence

228   of temperature, pressure, and ionic radius, and an elastic model for diffusion in silicates.

229   *Contrib. Mineral. Petrol.,* 141(6), 687-703 (2001).

230   22. Lambart, S. No direct contribution of recycled crust in Icelandic basalts. *Geochem. Perspect. Lett.*

231   4, 7-12 (2017).

232   23. Shorttle, O. Geochemical variability in MORB controlled by concurrent mixing and crystallization.

233   *Earth Planet. Sci. Lett.* 424, 1-14 (2015).

234   24. Hart, S., Blusztajn, J., Dick, H. J. B., Meyer, P. S., Muehlenbachs, K. The fingerprint of

235   seawater circulation in a 500-meter section of ocean crust gabbros. *Geochim. Cosmochim. Acta*

236   63, 4059–4080 (1999).

237   25. Barth, G. A., Mutter, J. C. Variability in oceanic crustal thickness and structure: Multichannel

238   seismic reflection results from the northern East Pacific Rise. *J. Geophys. Res.*101(B8), 17,951-

239   17,975 (1996).

240   26. Wang, T., Lin, J., Tucholke, B., Chen, Y. J. Crustal thickness anomalies in the North Atlantic

241   Ocean basin from gravity analysis, *Geochem. Geophys. Geosyst.* 12, Q0AE02 (2011).

242   27. Langmuir, C. H., Klein, E. M., Plank T. Petrological systematics of mid-ocean ridge basalts:

243   constraints on melt generation beneath ocean ridges. *Geophys. Monogr. Ser.* 71, 183-280

244   (1992).

245   28. Maclennan, J. Concurrent mixing and cooling of melts under Iceland. *J. Petrol.* 49, 1931–1953

246   (2008).

247   29. Wang, T., Tucholke, B. E., Lin., J. Spatial and temporal variations in crustal production at the

248   Mid-Atlantic Ridge, 25°N–27°30′N and 0–27 Ma, *J. Geophys. Res. Solid Earth,* 120, 2119–

249   2142 (2015).

250   30. Kogiso, T., Hirschmann, M. M., Reiners, P. W. Length scales of mantle heterogeneities and their

251   relationship to ocean island basalt geochemistry. *Geochim. Cosmochim. Acta* 68, 345-360 (2004).

252   31. Liu, B., Liang, Y. The prevalence of kilometer-scale heterogeneity in the source region of

253   MORB upper mantle. *Sci. Adv*. 3, e1701872 (2017).

254   32. Kelemen, P. B., Shimizu, N., Salters, V. J. M. Extraction of mid-ocean-ridge basalt from the

255   upwelling mantle by focused flow of melt in dunite channels. *Nature* 375, 747-753 (1995).

256   33. Spiegelman, M., Kelemen, P. B., Aharonov, E. Causes and consequences of flow organization

257   during melt transport: The reaction infiltration instability in compactible media. *J. Geophys.*

258   *Res.* 106(B2), 2061-2077 (2001).

259   34. Elliott, T., Spiegelman, M. 4.15 – Melt migration in oceanic crustal production: A U-Series

260   Perspective. In Holland, H. D. & Turekian, K. K. (eds) *Treatise on Geochemistry*, 2nd edn.

261   Oxford: Elsevier, pp. 543-581 (2014).

262   35. Lambart, S., Laporte, D., Provost, A., Schiano, P. Fate of pyroxenite-derived melts in the

263   peridotitic mantle: thermodynamical and experimental constraints. *J. Petrol.* 53 (3), 451–476

264   (2012).

265   36. Yaxley, G., Green, D.H. Reactions between eclogite and peridotite: mantle refertilisation by

266   subduction of oceanic crust. *Schweizerische Mineralogische und Petrographische Mitteilungen*

267   78(2), 243-255 (1998).

268   37. Weatherley, S. M., Katz, R. F. Melting and channelized magmatic flow in chemically

269   heterogeneous, upwelling mantle, *Geochem. Geophys. Geosyst.* 13, Q0AC18 (2012).

270   38. Weatherley, S. M., Katz, R. F. Melt transport rates in heterogeneous mantle beneath mid-ocean

271   ridges. *Geochim Cosmochim Acta*, 172, 39-54 (2016).

272   39. Anderson, D. L. The scales of mantle convection. *Techtonophysics* 284, 1-17 (1998).

273   40. Stixrude, L., Lithgow-Bertelloni, C. Geophysics of Chemical Heterogeneity in the Mantle.

274   *Annu. Rev. Earth Planet. Sci.* 40, 569-595 (2012).

275   41. Wanless, V. D., Shaw, A. M. Lower crustal crystallization and melt evolution at mid-ocean

276   ridges. *Nature Geosci.* 5, 651-655 (2012).

277   42. Delacour, A., Früh-Green, G. L., Frank, M., Gutjahr, M., Kelley, D. S. Sr- and Nd-isotope

278   geochemistry of the Atlantis Massif (30°N, MAR): Implications for fluid fluxes and lithospheric

279   heterogeneity. *Chem. Geol.* 254, 19-35 (2008).

280   43. Lehnert, K., Su, Y., Langmuir, C., Sarbas, B., Nohl, U. A global geochemical database structure

281   for rocks. *Geochem. Geophys. Geosyst*. 1, 1012 (2000).

282

292

Author contributions: JL designed the study. SL and JL wrote the manuscript with input from MAM, JK and GD. SL and JL selected the samples. SL and MC performed the element maps. SL performed trace element analyses and geochemical modelling. SL and JL performed micro-milling, and SL, JL, MAM and JK performed column chemistry and isotopic analyses.

297

Competing interests. The authors declare no competing interests.

299

Figure captions:

Fig. 1. Isotopic compositions of Atlantis Massif cumulate minerals. $^{87}Sr/^{86}Sr$ (a) and $^{143}Nd/^{144}Nd$ (b) ratios of clinopyroxene (green) and plagioclase (blue) cores of cumulate gabbroic rocks from IODP Hole U1309D, compared with whole rock (WR) isotopic analyses performed in this study (red symbols) and on gabbroic rocks recording less than 40% alteration[42] (black crosses). The grey bands represent the compositional variability of MORB analysed in this study and reported in the literature (PetDB database[43]) at the same latitude (30°N±1°). Error bars: 2SEE; mbsf = metres below seafloor.

308 **Fig. 2. Isotopic compositions of cumulate minerals, abyssal peridotites and MORB along the**

309 **northern MAR and results of geochemical modeling. a-b.** $^{87}Sr/^{86}Sr$ (a) and $^{143}Nd/^{144}Nd$ (b) ratios

310 measured in this study, in MORB (PetDB Database[43]) and in abyssal peridotites[7,12,13] from the

311 northern MAR. Red dotted lines show the latitude of the major hotspots affecting MORB

312 compositions[15]. Error bars: 2 SEE. In (b), the vertical dashed lines show the isotopic compositions

313 of the two mantle components used in calculations and the yellow circles are the average MORB

314 compositions per ridge segment. **c.** Calculated fraction of recycled, material-derived melt in the

315 averaged MORB. **d.** Comparison of the calculated crustal thicknesses generated by varying the

316 proportion of recycled material and the potential temperature (dashed green line) with the averaged

317 elevations of the collected MORB (orange line).

318 **Fig. 3. Intrasample heterogeneity.** $^{143}Nd/^{144}Nd$ ratios of plagioclase (black circles) and

319 clinopyroxene (colored circles) as a function of the anorthite (An) content of the plagioclase in the

320 sample. Analyses from individual samples are connected by black tie lines. The blue line and field

321 show the average and 2σ composition of the cumulate minerals. The red line and field show the

322 average composition and 2σ of MORB (basalts, diabase and microgabbros).

323 **Fig. 4. Frequency distribution of Nd isotopic compositions.** Comparison between plagioclase and

324 clinopyroxenes from primitive cumulates (this study) and North Atlantic MORB (grey: all data;

325 yellow: MORB not affected by hot spots[15]).

326 **Fig. 5. Illustration of magma delivery from a two-component mantle to the crust.** The fusible

327 and enriched recycled material (in red) starts to melt at higher pressure than the depleted peridotite.

328 Both lithologies nucleate their own network of high-permeability channels, facilitated by melt-rock

329 reaction[35,36] and thermal diffusion[37,38], and by mechanical[30] and/or chemical[33] instabilities,

330 respectively. Generation of separate networks limits magma mixing and help to deliver a larger

331 isotopic variability to the crust. The shallowest axial magma chamber host a larger volume of

332   magma where mixing and crystallization continue, resulting in the loss of much of the primary

333   mantle diversity.

334

335   **Methods**

336   *Geological setting and sample selection*

337   The Atlantis Massif is a 1.5-2 Myr old oceanic core complex on the western rift flank of

338   Mid-Atlantic Ridge 30°N. IODP Sites U1309, U1310 and U1311 were drilled during Expeditions

339   304 and 305. The main hole, Hole U1309D, penetrated 1415.5 mbsf and recovery averaged 75%.

340   Over 96% of Hole U1309D is made up of gabbroic rock types, which are amongst the most

341   primitive as well as freshest plutonic rocks known from the ocean floor[16].

342   We selected 74 samples from the core U1309D samples to cover the entire drill hole,

343   including 28 olivine gabbros, 8 troctolites, 7 olivine-rich troctolites, 11 gabbros, 4 oxide gabbros, 2

344   gabbronorites, 6 microgabbros and 7 diabases. We also collected 9 basalt and glass samples

345   recovered at IODP sites U1310 and U1311.

346

347   *Element maps and selection of mineral for isotopic analyses*

348   Forty of the selected samples were polished and carbon-coated to perform major and minor

349   element maps. Element maps were obtained at Cardiff University on a Zeiss Sigma HD FEG-SEM

350   equipped with dual Oxford Instruments X-max 150 mm^2 energy dispersive silicon drift detectors.

351   We used an acceleration voltage of 20 kV and a dwell time of 9 ms. The beam current and aperture

352   were adjusted to obtain optimum output count rates of ~410,000 cps, enabling rapid mapping of

353   large proportions of the samples at high spatial resolution (step size 20 μm). Raw counts were

354   background corrected using Oxford Instrument's AZtec software, which was then used to generate

355   multi-element maps.

356   From these element maps, we selected primitive, fracture and inclusion free, plagioclase

357   (high anorthite, An, content) and clinopyroxene (high Mg# and low TiO_2/Cr_2O_3 ratio) cores for

358   micromilling (Supplementary Fig. 1). We also preferentially selected large minerals (when

359   possible) to limit the depth of each drill hole and the number of holes required to collect the

360   sufficient amount of material for Nd isotopic analysis. Finally, we carefully examined every

361   selected drilling area for fractures or inclusions and redefined the drilling area accordingly.

362

363   *LA-ICP-MS measurements and estimations of the Nd and Sr content of the sample*

364   We determined trace element concentrations on the selected clinopyroxenes and

365   plagioclases using laser ablation inductively coupled plasma mass spectroscopy (LA-ICP-MS).

366   Analyses were performed at Cardiff University on a New Wave research UP213 UV laser system

367   attached to a Thermo X Series 2 ICP-MS. Each mineral underwent two analyses (by lines) to allow

368   mineral compositional variability to be assessed. A minimum length of 300 μm and a beam

369   diameter of 80 μm were used, with a laser operating at 10 Hz frequency and sample translation at 6

370   μm s^{-1}. Acquisition time was about 80s (20s gas blank, >50 s acquisition, 10s washout)

371   We used the silicate glass standard NIST 612 as reference material, and clinopyroxene and

372   plagioclase Ca contents, measured by SEM-EDS, served as internal standard. We tested the

373   accuracy of the measurement with two external standards (BIR and BCR-2G) analyzed every 10

374   samples. Based on 10 BRC-2G measurements, the relative errors on the trace element contents lie

375   between 0.3 and 15%, with 3.8% and 5.2% for Nd and Sr respectively (Supplementary Fig. 3).

376

377   *Micro-sampling via Micro-mill*

378   Micromilling of the samples was performed in the Faculty of Sciences at Vrije Universiteit

379   Amsterdam (VUA) and in the School of Earth and Ocean Sciences at Cardiff University. We used a

380   procedure adapted from the that described by Charlier et al.[44] for thick sections. Polished billets

381   were first placed in an ultrasonic bath of Milli-Q water (standard purity with a final resistivity of

382   >18.4 MΩ) for 20 min, and then cleaned with acetic acid for one minute and finally cleaned and

383 dried with ethanol. Drill bits were also cleaned between each sampling in 0.165HCl for 2s and then

384 in an ultrasonic bath of Milli-Q water for 10min.

385   We placed 2-3 drops of Milli-Q water on the area to be drilled. The drilled material is

386 brought in suspension as the drilling proceeds. When the solution becomes saturated, it was pipetted

387 into a Teflon vial previously cleaned for isotope chemistry and new drops of Milli-Q water were

388 added to the drilling area. During the whole drilling procedure, we made sure that Milli-Q water

389 was always present on the drilling area. Finally, at the end of the drilling sequence, all the water on

390 the sample was collected.

391   After the micromilling was complete, we estimated the sampled volume by measuring the

392 surface area and the depth of the hole. We also checked for the presence of inclusions. This gave us

393 a maximum estimate of the volume of material collected, as not all the drilled material is recovered.

394 Total procedural blanks were performed by simulating a 60min milling sequence on a clean sample.

395 A clean drill bit was immersed into Milli-Q water on the rock slab sample, and the water was

396 collected and resupplied following the same procedure than a regular micro-milling sequence in

397 order to collect a similar amount of water. The blanks were then processed by column chemistry

398 following the same procedure as the samples (see below).

399

400 *Column chemistry*

401 *Separation of Sr and Nd from plagioclase and clinopyroxene cores*

402   Column chemistry on plagioclase and clinopyroxene powders was performed at VUA and in

403 the CELTIC laboratory at Cardiff University. Samples were dissolved in Teflon vials in a 4:1 mix

404 of HF and HNO_3 on a hotplate at 140 °C for 3 days. Sr and rare earth elements (REEs) were

405 separated from the matrix in a setup whereby Sr Resin columns (Eichrom, 50 μl resin) are placed

406 directly above TRU Resin columns (Eichrom, 150 μl resin). By placing the Sr column above the

407 TRU Resin column during loading and washing, the pre-fraction from the Sr Resin column (in 3 M

408 HNO3) was directly eluted onto the TRU Resin column, after which the two column sets were

409   separated and Sr and REE were eluted. Finally, the Nd was further separated from the other REE in

410   a Ln-Resin column procedure (see Fig. 5 in Koornneef et al.[45] for details). Due to the large sample

411   size needed for Nd isotope analyses for plagioclase, most Sr plagioclase samples were subjected to

412   a second pass of Sr chemistry.

413   Total procedural blanks varied between 38 and 43 pg for Sr and 2 and 12 pg for Nd. The

414   blanks were determined by isotope dilution using an ^{84}Sr spike and a ^{150}Nd spike respectively.

415

416   *Separation of Sr and Nd on whole rock*

417   We performed whole rock (WR) isotopic analyses on six diabase samples, five

418   microgabbros and one olivine-rich troctolite from the core U1309D, as well as on eight basalts and

419   one basaltic glass recovered from IODP sites U1310 and U1311 (see Supplementary Figure 1 for

420   locations of the drill cores). Column chemistry was performed in the CELTIC laboratory at Cardiff

421   University. Samples were crushed into an agate ball mill grinder and we collected between 200 and

422   300 mg . All but the glass sample (1310-A1-13-19) were leached in hot 6 M HCl for 3 h and then

423   rinsed to remove unbonded Sr[46]. The glass powder was leached at room temperature in 6 M HCl for

424   30 min. After centrifugation of the samples, the supernatant was discarded and samples were

425   washed in MQ, centrifuged again and the supernatant was again discarded. Residual powders were

426   then digested in hot concentrated HNO_3 and HF for 24 h, dried down, taken up in 1 mL of

427   concentrated HNO_3 and dried down again before being redissolved in 8 M HNO_3, and centrifuged.

428   Sr was separated in a double pass through a 1 mL pipette-tip column containing Sr-spec

429   resin. Samples were loaded in 8 M HNO_3 and sample matrix (including Ca and Rb) was removed in

430   the same acid. Sr was then collected in 0.05M HNO_3[47]. Samples were dried again and sequentially

431   brought into solution in concentrated HNO_3 and HCl, refluxed on a hotplate for at least 24 h, and

432   finally dried down prior to being brought into solution in dilute HCl.

433   Nd was separated in two steps. The REE were first separated from the sample matrix using

434   columns filled with a cation exchange resin (BioRad AG50W-x8, 2.5 mL). The REE fraction was

435   then dried and Nd was separated using columns filled with Ln-Spec resin (Eichrom, 1.1 mL)[48].

436   Total procedural blanks were 10 and 15 pg for Sr and Nd, respectively.

437

438   *Mass spectrometry*

439   *Clinopyroxene and plagioclase samples*

440   Sr and Nd analyses on plagioclase and clinopyroxene cores were performed on a Thermo

441   Scientific Triton-Plus TIMS at VUA. Samples and standards were loaded on outgassed Re

442   filaments in a clean air flow unit. Strontium analyses were performed using annealed Re filaments

443   in a single filament set-up whereas for Nd analyses annealed and zone-refined Re filaments were

444   used in a double filament configuration for the evaporation and ionisation positions,

445   respectively[45,49]. Isotope analyses were performed using 10^{11} Ω amplifiers in the feedback loop of

446   the Faraday detectors. Six of the current amplifiers installed in the TRITON Plus at VU Amsterdam

447   have the conventional 10^{11} ohm resistors, whereas the other 4 amplifiers are equipped with 10^{13}

448   ohm resistors. The Sr and Nd collection measurements reported here were carried out using the

449   same static analytical approach as Koornneef et al.[49].

450   The estimated amount of Nd and Sr analyzed, as well as the number of cycles for each

451   analysis, are reported in Supplementary Table 1. An 11 min baseline was measured during heating

452   of the sample and subtracted online from the raw intensity values. In most cases, analyses were run

453   to exhaustion. On average, we acquired 194 and 214 cycles for Sr isotopic analyses in plagioclase

454   and clinopyroxenes, respectively, and 85 and 97 cycles for Nd isotopic analyses in plagioclase and

455   clinopyroxene, respectively.

456   The intensities on the 87 Mass are corrected for minor ^{87}Rb contributions by using the

457   canonical ^{87}Rb/^{85}Rb of 0.3857. Sm was not detected for all but three clinopyroxenes (149R2-68-

458   71a, 252R4-3-6a and 257R1-95-100a). For the three clinopyroxenes where we detected ^{147}Sm we

459   correct the 144 intensity using $^{144}Sm/^{147}Sm$ = 0.20502. Nd and Sr measurements are subsequently

460   corrected for instrumental mass fractionation by using the exponential law, and $^{146}Nd/^{144}Nd$ =

461   0.7219 and $^{86}Sr/^{88}Sr$ = 0.1194, respectively. To test the accuracy of the measurements, 7-8 mg of

462   BHVO-2 standards were passed through the complete chemical procedure. Filaments were loaded

463   with either 2 or 10 ng of Nd, and with 200ng of Sr. Data are within the error of the preferred values

464   reported in GeoReM database (Supplementary Fig. 4).

465

466   *Whole rock*

467   Sr and Nd isotope ratios were measured on a Nu Instruments multi-collector (MC)-ICP-MS

468   system in the CELTIC laboratory at Cardiff University in static mode. Sr isotopic measurements

469   were normalized internally to $^{86}Sr/^{88}Sr$ = 0.1194 and NBS-987 was run every five samples as a

470   secondary correction to account for small variations in non exponential mass bias. ^{86}Kr

471   interferences were below background level, therefore no correction was made. Nd isotopic

472   measurements were normalized internally to $^{146}Nd/^{144}Nd$ = 0.7219 and JNd-i was run every five

473   samples a secondary correction to account for small variations in non exponential mass bias.

474   Accuracy of the measurements was tested using JB-2 as a secondary standard that was passed

475   through the complete chemical procedure and the Sr and Nd isotopic ratios obtained are

476   indistinguishable within error from the preferred values reported in GeoReM database

477   (Supplementary Fig. 5).

478

479   *Calculation of the contribution of the recycled material to the parental melts and fraction of*

480   *recycled material-derived melt in parental melts*

481   For the enriched component, we used the isotopic ratio of the most enriched clinopyroxene analysed

482   in this study ($^{143}Nd/^{144}Nd$ = 0.512800 ± 15; $^{87}Sr/^{86}Sr$ = 0.702884 ± 9). Such isotopic signature can

483   be reproduced by partial melting of a ~ 1.1 Ga recycled gabbro[50] (Supplementary Fig. 2). We used

484   the same major and trace element composition used to calculate the age, i.e. the average oceanic

485 gabbro composition estimated by Hart et al.[24]. For the depleted component, we used the isotopic

486 ratio of the most depleted abyssal peridotite reported along the MAR (Vema lithospheric section[7],

487 $^{143}Nd/^{144}Nd = 0.51366$) and major and trace element compositions of the depleted endmember of

488 the depleted MORB mantle (D-DMM[51]). To estimate the fractions of each end-member in the

489 parental melts of cumulate minerals, we need to know the Nd content of melt generated by each

490 end-member. Following the approach used by Lambart et al.[22], we considered that the mantle

491 follows an adiabatic path, with a potential temperature of $T_P = 1300°C$. Both components are in

492 thermal equilibrium and chemically isolated. We used Melt-PX[52] to calculate the Pressure (P) –

493 Temperature (T) - Melt fraction (F) path. We considered that both lithologies were chemically

494 isolated but in thermal equilibrium. Calculations performed with Melt-PX take into account heat

495 transfer between the different lithologies. Calculations were stopped when the mantle column had

496 upwelled to the base of the crust, i.e. when the pressure at the base of the crust, $P_c = P$. The initial

497 fraction of recycled gabbro in the mantle source (i.e., 5%) was chosen such that a 5-6 km crust

498 thickness was generated[29]. We used alphaMELTS[53] to calculate the mineral assemblage at each

499 pressure step (i.e., every 100 bars) for each lithology. We calculated the Nd content of the melt

500 derived from each lithology along the adiabatic path using incremental batch melting calculations,

501 integrating the liquid produced over the melting region and dividing by the total volume produced

502 (see Lambart[22] for details on calculations). Accumulated Nd content of the melt derived from the

503 recycled crust ($[Nd]_{RC}$) and DDMM ($[Nd]_{DDMM}$) are 8.1 and 2.7ppm, respectively. We can solve for

504 the fraction of recycled crust (F_{RC}) required to explain the isotopic mineral compositions such as:

505 $^{143}Nd/^{144}Nd_{cpx/plag} = (F_{RC} \times [Nd]_{RC})/(F_{RC} \times [Nd]_{RC} + (1- F_{RC}) \times [Nd]_{DDMM}) \times {}^{143}Nd/^{144}Nd_{RC} +$

506 $(1 - (F_{RC} \times [Nd]_{RC})/(F_{RC} \times [Nd]_{RC} + (1 - F_{RC}) \times [Nd]_{DDMM})) \times {}^{143}Nd/^{144}Nd_{DDMM}$

507

508 *Nature of the enriched component.*

509 As noted above, we assumed that the lowest $^{143}Nd/^{144}Nd$ ratio is produced by partial melting of a ~

510 1.1 Ga recycled gabbro[50]. However, other processes can produced similar isotopic ratios, such as a

511   small contribution of recycled sediments[50] or the partial melting of hybrid lithologies resulting from

512   the mixture between older recycled material and peridotite. Contribution of sediments is

513   accompanied by strong enrichments in $^{87}Sr/^{86}Sr$ and $^{176}Hf/^{177}Hf$, which are difficult to reconcile

514   with the observed MORB array[50]. To investigate the effect of the nature of the enriched material on

515   our calculations, we performed an additional set of calculations using a hybrid lithology, produced

516   by a 1:1 mix between recycled gabbro and depleted peridotite. We used KG1[54] for the major

517   elelemt composition and calculated trace elelement composition as a 1:1 mixture between the

518   oceanic gabbro[24] and D-DMM[51]. The most enriched clinopyroxene Nd isotopic ratio can be

519   reproduced assuming the recycled gabbro is ~1.3 Ga[50]. The calculated Nd content of the

520   accumulated melt derived from KG1 is 3.8ppm. Solving for the fraction of KG1 in the melt, we

521   obtained significantly higher (48 to 75%) contribution of KG1-derived melt in the aggregated

522   magma. Using the estimated fraction of KG1 in the melt, we calculated the corresponding fraction

523   in the source. We can then estimate the proportion of recycled crust in the mantle simply using the

524   relationship $X_{RC}^{source} = 0.5\ X_{KG1}^{source}$. Both calculations produce similar profiles of thickness

525   variation (Supplementary Fig. 6c). However, for $T_P = 1300°C$, calculations using KG1 yield to a

526   proportion of recycled crust between 9 and 21% (Supplementary Fig. 6e). These estimations are

527   significantly higher than previous estimation for the amount of recycled crust in the mantle source

528   of MORB[55,56]. In summary, the enriched signature can reflect either the direct participation of

529   crustal material (i.e., by partial melting) or its indirect participation, by interaction with the

530   surrounding peridotite and subsequent melting of an "enriched" peridotite/hybrid lithology.

531   However, because of the higher solidus temperatures of peridotite or hybrid lithology such as KG1

532   in comparison to the recylced crust[51], the proportion of enriched material in the mantle required to

533   reproduce the enriched melt composition is significantly higher in the latter case, resulting to a

534   higher initial proportion of recycled crust needed to produce this enriched composition.

535

536   *Condition for the preservation of the mantle component isotopic signatures.*

537 The recycled crust has a higher melt productivity[52] and Nd abundance[24] than the peridotite[51].

538 Hence, even a small degree of mixing will dilute the signature of the most depleted component.

539 Inversely a small contribution of depleted peridotite melt to the recycled crust-derived melt will not

540 significantly affect the isotopic composition of the latter, and aggregated melts are more likely to

541 sample the enriched end-member composition. In fact, 14% of recycled crust-derived melt in the

542 aggregated magma is required to change the Nd isotopic ratio of the melt from 0.51366 to 0.51332

543 (i.e, from the most depleted abyssal peridotite[7] to the most depleted cumulate mineral). However, a

544 14% addition of peridotite melt to the recycled crust-derived melt would only change its isotopic

545 ratio from 0.51280 to 0.51283 (i.e, unchanged within error). Hence, while the isotopic composition

546 of the depleted end-member is most likely to be diluted, the most enriched composition observed in

547 cumulate minerals is a good representative of the enriched end-member in the mantle beneath the

548 Atlantis massif.

549

550 **Code availability.** The code used to calculate adiabatic melting of a two component mantle source,

551 Melt-PX[52], can be accessed at https://doi.org/10.1002/2015JB012762 .

552

553 **Data availability.** The authors declare that data supporting the findings of this study are available

554 within the paper, the Methods and in the PetDB data repository

555 (http://www.earthchem.org/petdbWeb/search/readydata/MAR55S-52N_major_trace_isotope.csv).

556

557 **References**

558 44. Charlier, B. L. A. et al. Methods for the microsampling and high-precision analysis of strontium

559   and rubidium isotopes at single crystal scale for petrological and geochronological applications.

560   *Chem. Geol.* 232, 114-133 (2006).

561 45. Koornneef, J. M. et al. TIMS analysis of Sr and Nd isotopes in melt inclusions from Italian

562   potassium-rich lavas using prototype 10^{13} Ω amplifiers. *Chem. Geol.* 397, 14-23 (2015).

563 46. Millet, M. –A., Doucelance, R., Schiano, P., David, K., Bosq, C. Mantle plume heterogeneity

564   versus shallow-level interactions: A case study, the São Nicolau Island, Cape Verde

565   archipelago. *J. Volcanol. Geotherm. Res.* 176, 265–276 (2008).

566 47. McGee, L. E., Smith, I. E., Millet, M. -A., Handley, H. K., Lindsay, J. M. Asthenospheric

567   control of melting processes in a monogenetic basaltic system: A case study of the Auckland

568   Volcanic Field, New Zealand. *J. Petrol.* 54(10), 2125-2153 (2013).

569 48. McCoy-West, A. J., Millet, M. -A., Burton, K. W. The neodymium stable isotope composition

570   of the silicate Earth and chondrites. *Earth Planet. Sci. Lett.* 480, 121-132 (2017).

571 49. Koornneef, J. M., Bouman, C., Schwieters, J. B., Davies, G. R. Use of 10^{12} ohm current

572   amplifiers in Sr and Nd isotope analyses by TIMS for application to sub-nanogram samples. *J.*

573   *Anal. At. Spectrom.* 28, 749-754 (2013).

574 50. Stracke, A., Bizimis, M., Salters, V. J. M. Recycling oceanic crust: Quantitative constraints.

575   *Geochem. Geophys. Geosyst.* 4(3), 8003 (2003).

576 51. Workman, R. K., Hart, S. R. Major and trace element composition of the depleted MORB

577   mantle (DMM). *Earth Planet. Sci. Lett.* 231, 53–72 (2005).

578 52. Lambart, S., Baker, M. B., Stolper, E. M. The role of pyroxenite in basalt genesis: Melt-PX, a

579   melting parameterization for mantle pyroxenites between 0.9 and 5GPa. *J. Geophys. Res. Solid*

580   *Earth* 121, 5708–5735 (2016).

581 53. Smith, P.M., Asimow, P.D. Adiabat_1ph: A new public front-end to the MELTS, pMELTS, and

582   pHMELTS models. *Geochem. Geophys. Geosyst.* 6, Q02004 (2005).

583 54. Kogiso, T., Hirose, K., Takahashi, E. Melting experiments on homogeneous mixtures of

584   peridotite and basalt: application to the genesis of ocean island basalts. *Earth Planet. Sci. Lett.*

585   162, 45-61 (1998).

586 55. Hirschmann, M. M., Stolper, E.M. A possible role for garnet pyroxenite in the origin of the

587   "garnet signature" in MORB. *Contrib. Mineral. Petrol.* 124, 185-208 (1996).

588   56. Sobolev, A.V. et al. The amount of recycled crust in sources of mantle derived melts. *Science*

589   316, 590–597 (2007).
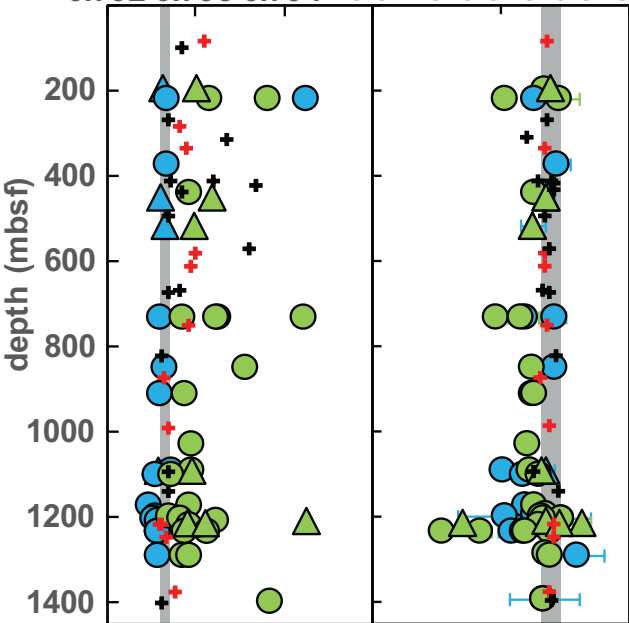
Legend:

This study

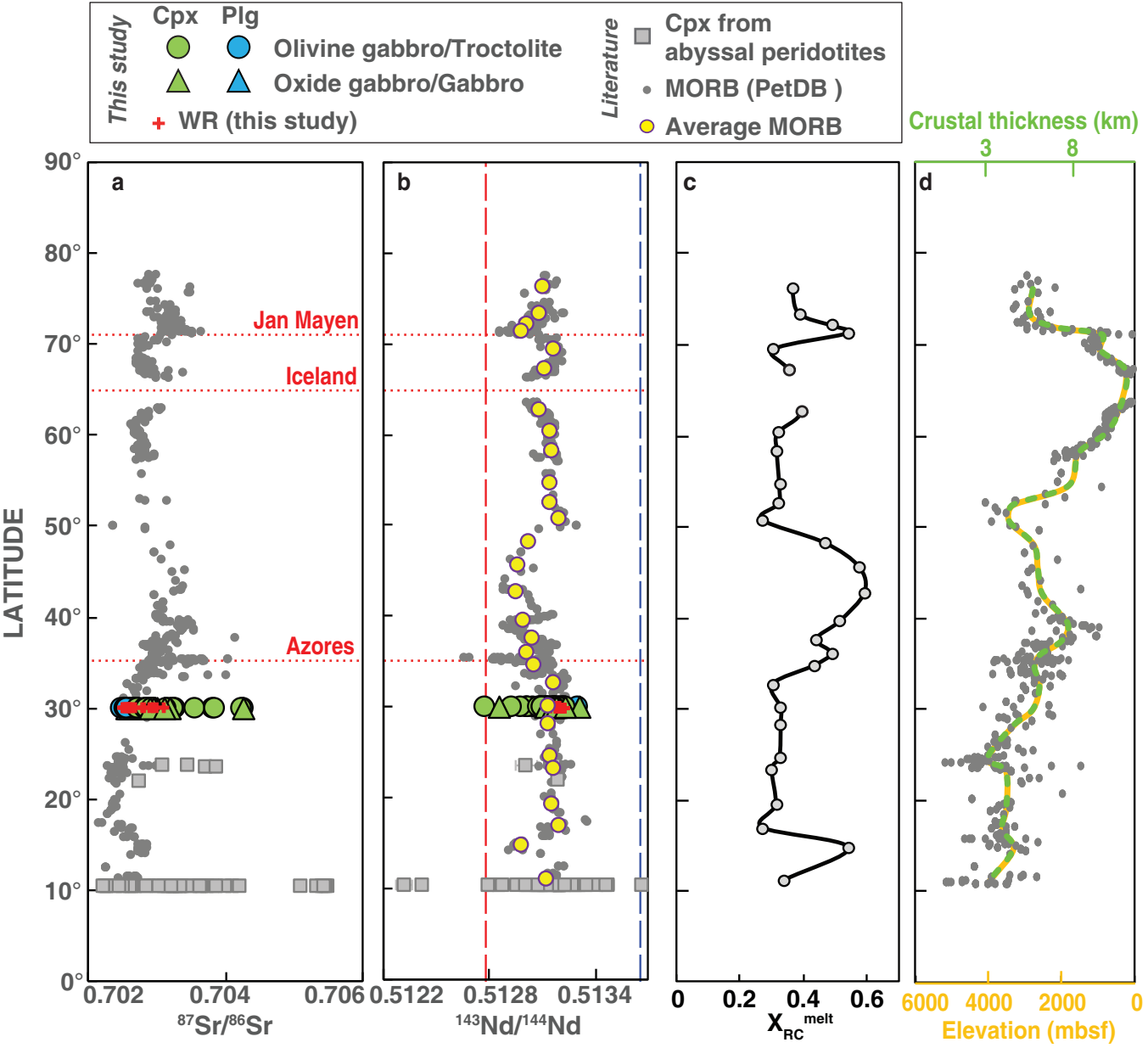Cpx — ● Olivine gabbro/Troctolite — △ Oxide gabbro/Gabbro (green)
Plg — ● Olivine gabbro/Troctolite — △ Oxide gabbro/Gabbro (blue)
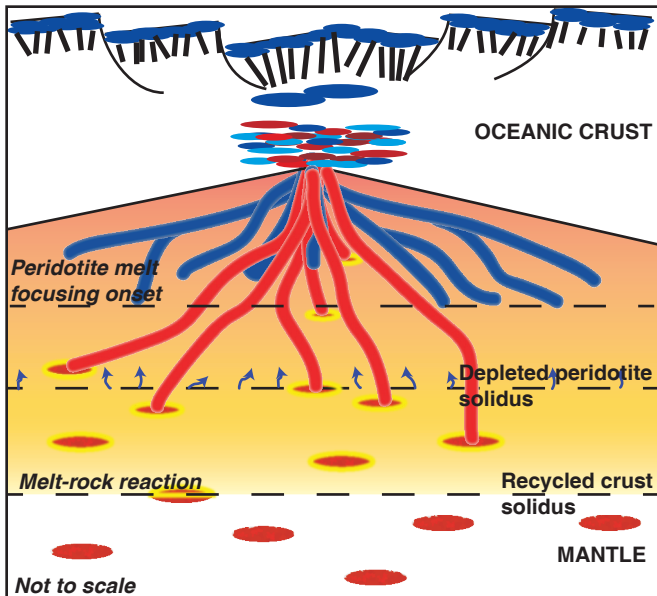+ WR (this study)
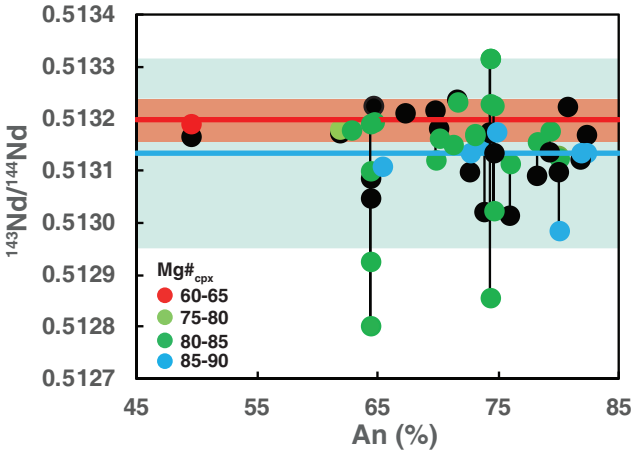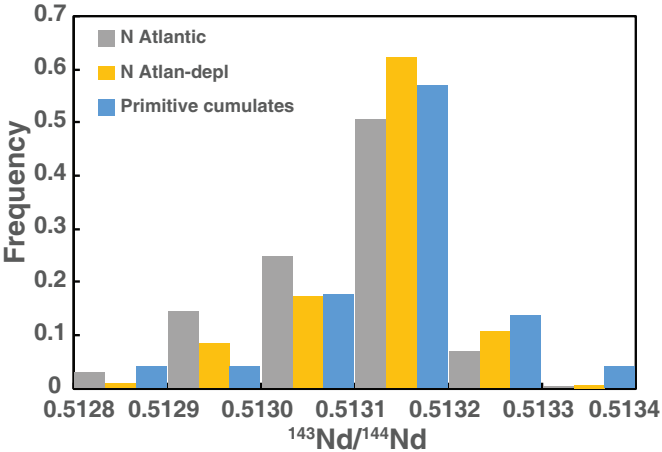
Literature

■ Cpx from abyssal peridotites
• MORB (PetDB)
● Average MORB

a $^{87}Sr/^{86}Sr$

Jan Mayen
Iceland
Azores

b $^{143}Nd/^{144}Nd$

c X_{RC}^{melt}

d Crustal thickness (km)
3   8
Elevation (mbsf)
6000 4000 2000 0

LATITUDE
90°
80°
70°
60°
50°
40°
30°
20°
10°
0°

OCEANIC CRUST

Peridotite melt
focusing onset

Depleted peridotite
solidus

Melt-rock reaction

Recycled crust
solidus

MANTLE

Not to scale
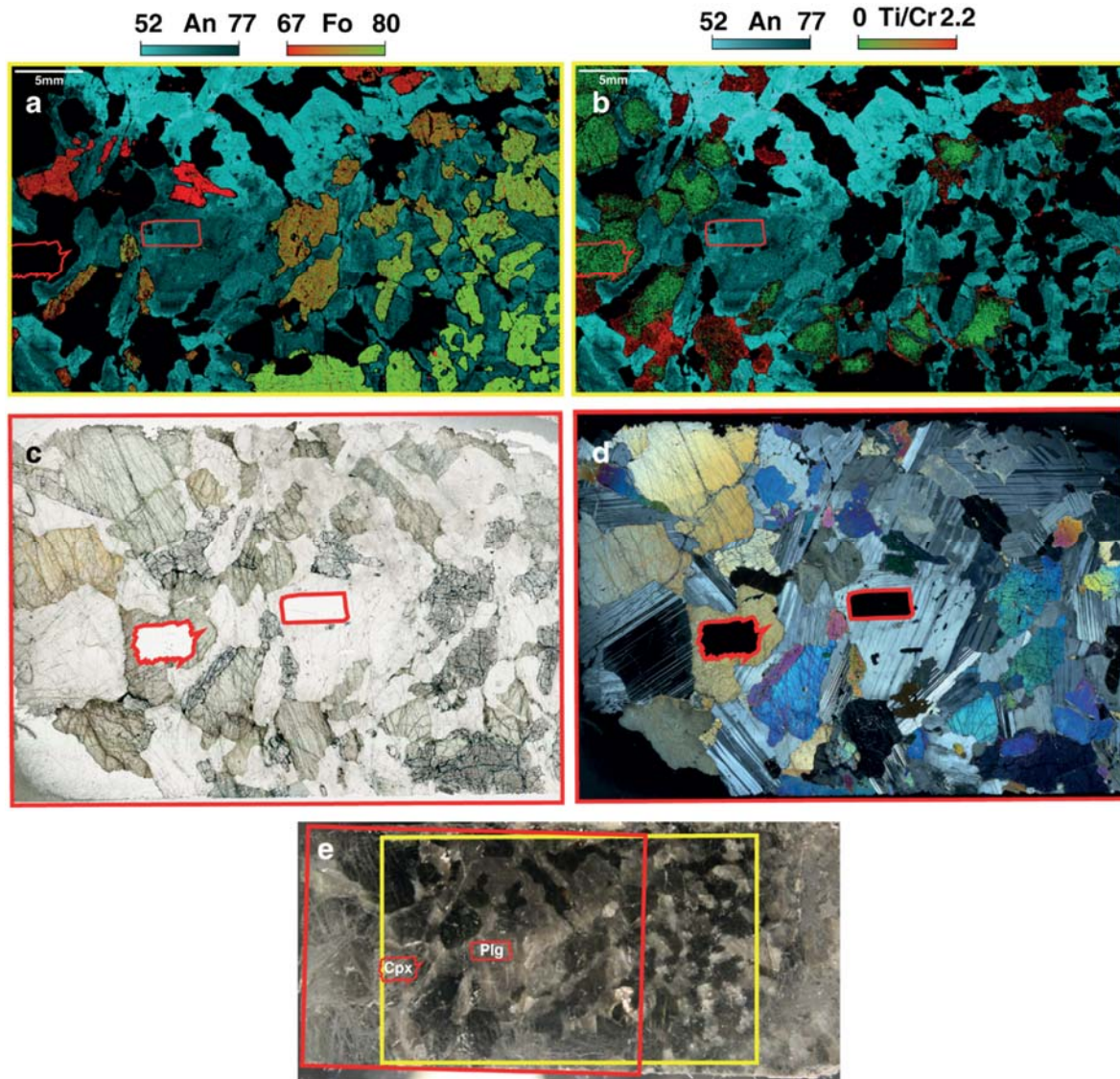
Supplementary Figure 1. Illustration of the method for selecting micro-milling sites. Mg–Fe–Na **(a)** and Ti-Cr-Na **(b)** element maps, photomicrographs **(c-d)** showing the microdrill locations, and core photo **(e)** showing the element map area (yellow), the thin section area (red) of the olivine gabbro 268R3-6-12 from IODP Hole U1309D. Map (a) shows Fo (red to green) and An (light to dark blue) content variations of olivine and plagioclase at the scale of the sample. Clinopyroxene appears black because Fe and Mg have been scaled to show the olivine compositions. Map (b) highlight An content of plagioclase and TiO_2/Cr_2O_3 ratio in clinopyroxene. Red highlighted area indicate microdrill location. A noteworthy feature is the substantial An, Fo and TiO_2/Cr_2O_3 variations on a cm scale (a-b).
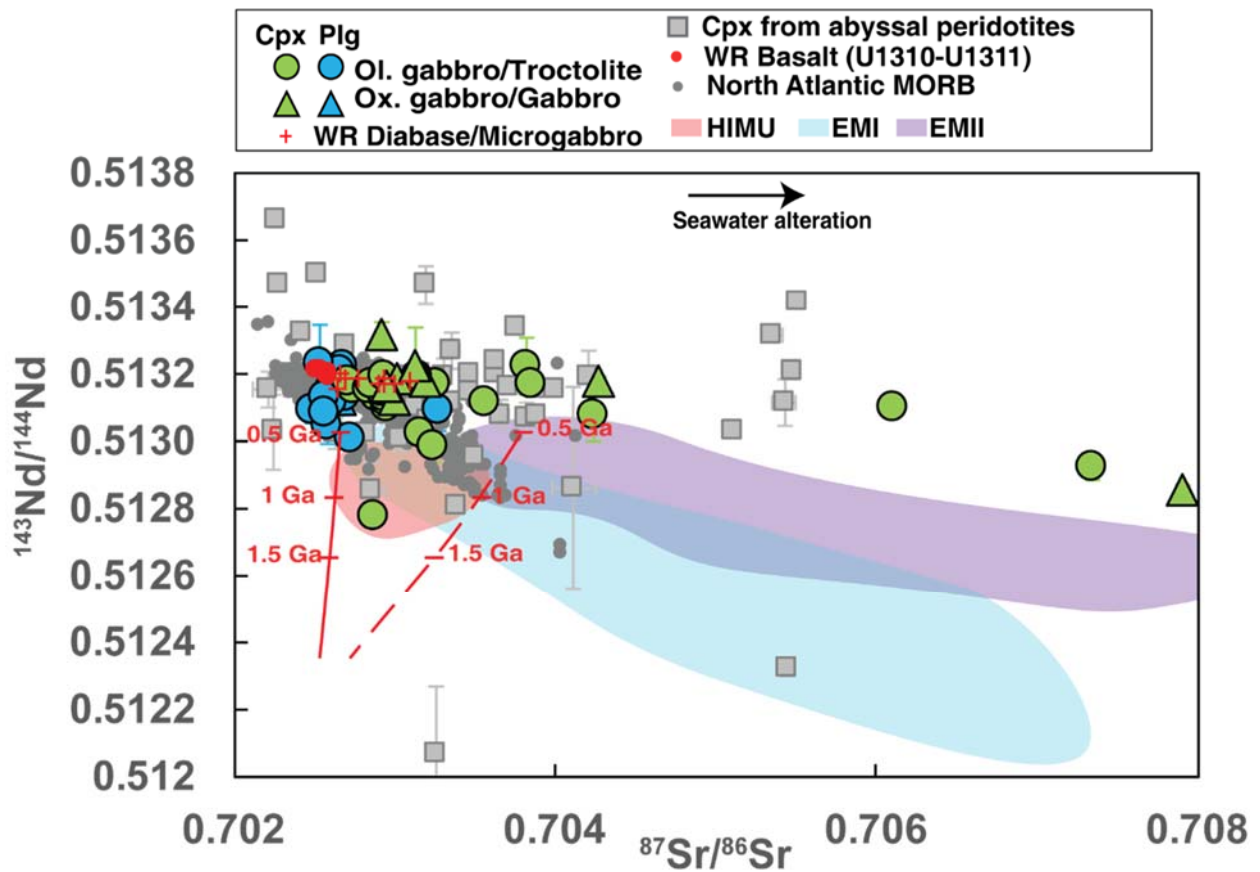
Supplementary Figure 2. Comparison between isotopic compositions analysed in this study and compositions of North Atlantic MORB. [143]Nd/[144]Nd versus [87]Sr/[86]Sr ratios of Atlantis Massif clinopyroxene and plagioclase compared with whole rock (WR) diabase and basalt isotopic analyses performed in this study, theNorth Atlantic MORB compositions reported in the literature (PetDB database[42]) and the clinopyroxene compositions from abyssal peridotites collected along the MAR[7,12,13]. Compositional fields of HIMU (red), EMI (blue) and EMII (purple) basalts are shown for comparison[50]. The red lines are calculated present-day isotopic compositions of recycled oceanic gabbro affected (dashed line) or not (solid line) by seawater alteration, as a function of recycling age[50]. Error bars: 2SEE.
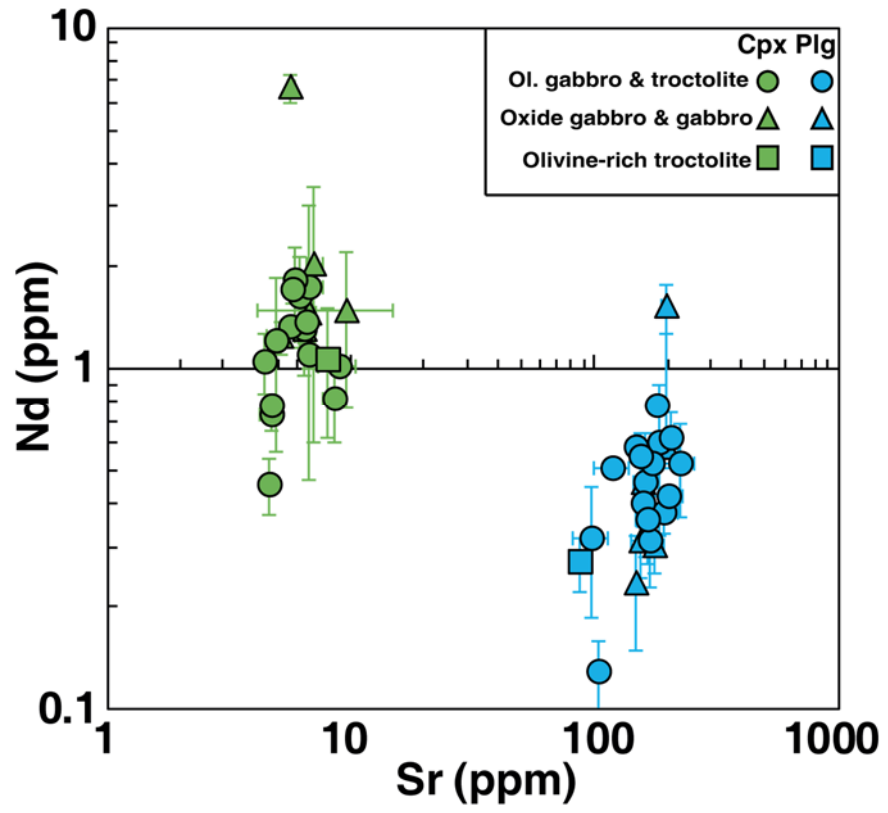
Supplementary Figure 3. Sr and Nd concentrations in selected minerals for micromilling (2σ error bars).
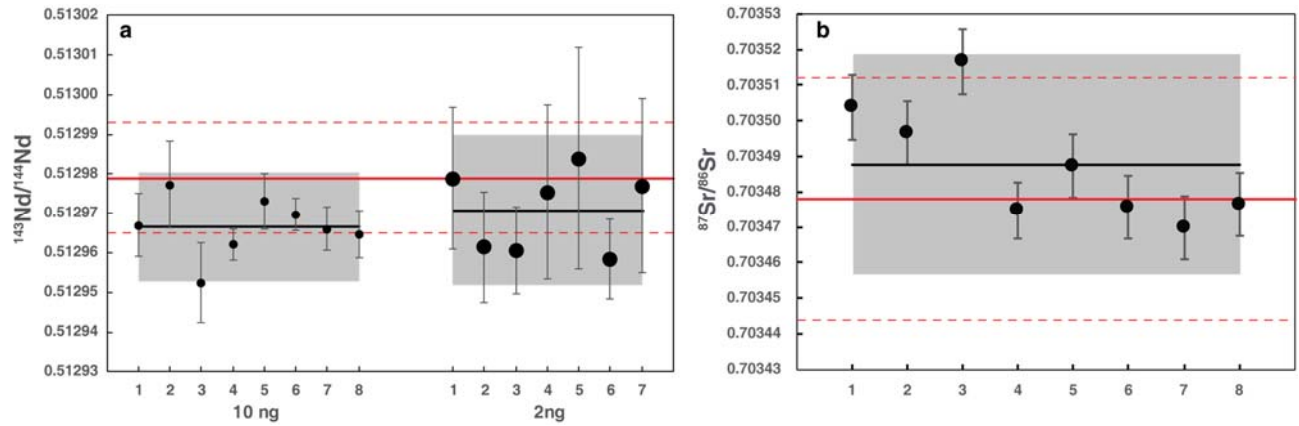
Supplementary Figure 4. Standard analyses on TIMS. a. ^{143}Nd/^{144}Nd ratios (2SE error bars) measured on BHVO-2. Filaments were loaded with 10 ng (small circles) or 2 ng of Nd (large circles). **b.** ^{87}Sr/^{86}Sr ratios (2SE error bars) measured on 200ng Sr separated from BHVO-2. Black line and grey band are the average and 2SD measured on BHVO-2 in this study. Solid and dashed red lines are average and 2SD reported for BHVO-2 in GeoReM database.
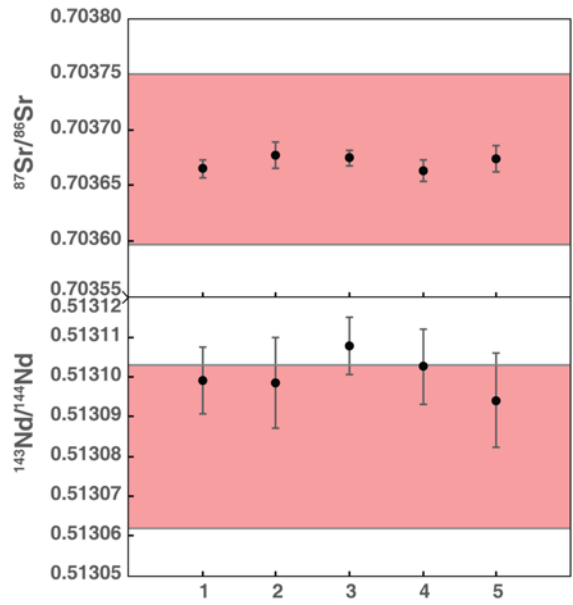
Supplementary Figure 5. Standard analyses on Nu Instrument. $^{87}Sr/^{86}Sr$ and $^{143}Nd/^{144}Nd$ ratios measured on JB-2 after correction for fractionation and mass bias (2SE error bars). Red bands are the range of values reported for JB-2 in GeoReM database.
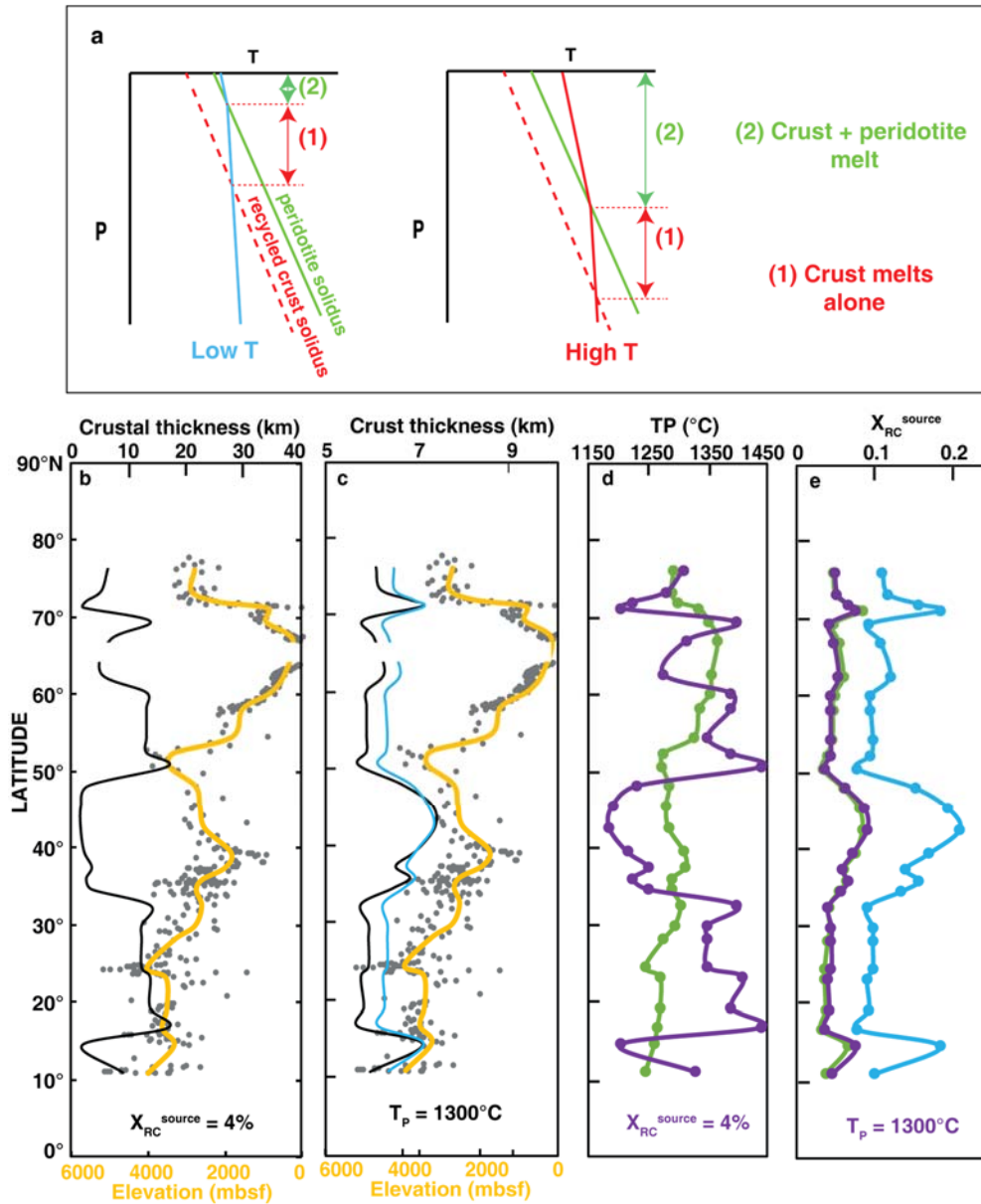
Supplementary Figure 6. Results of geochemical modelling. a. Schematic illustration of the effect of mantle potential temperature (T_P) on the fraction of recycled crust in the melt: increasing T_P decreases the ratio between the interval where only the recycled crust is melting and the interval where both crust and peridotite are melting (i.e., (1)/(2) ratio). **b-c.** Comparison between the average MORB elevations (orange line) with the calculated crust thicknesses (black line), assuming a constant fraction of recycled crust, $X_{RC} = 4\%$, and varying T_P (b), or assuming a constant $T_P = 1300°C$ and varying the proportion of recycled crust (c). **d.** Calculated T_P with constant $X_{RC} = 4\%$ (purple) and the hybrid model (green). **e.** Calculated X_{RC}^{source} with constant $T_P = 1300°C$ (purple) and with the hybrid model (green). In (c) and (e), the blue line shows the results using $T_P = 1300°C$ and the composition KG1 for the enriched material.

Supplementary Table 1. Isotopic analyses of clinopyroxenes, plagioclase and whole rocks plotted in Figs. 1&2.

Sample	depth (mbsf)	Plagioclase $^{87}Sr/^{86}Sr$	Sr*	n	$^{143}Nd/^{144}Nd$	Nd*	n	Clinopyroxene $^{87}Sr/^{86}Sr$	Sr*	n	$^{143}Nd/^{144}Nd$	Nd*	n	Whole rock $^{87}Sr/^{86}Sr$	$^{143}Nd/^{144}Nd$
15R1-43-45	84.54													0.703096 (9)	0.513184 (8)
36R1-48-53	196.09	0.702643 (8)	200	185	0.513169 (30)	8	114	0.703023 (10)	35	208	0.513191 (9)	30	168		
41R2-27-31a	221.25	0.702693 (8)	200	200	0.513136 (20)	2	96	0.703158 (14)	50	212	0.513024 (16)	4	181		
41R2-27-31b	221.50	0.704276 (44)	200	95				0.703823 (36)	50	54	0.513226 (87)	5	54		
54R3-125-126	285.15													0.702825 (10)	
65R1-141-143	335.42													0.702905 (11)	0.513169 (11)
73R2-124-129	375.12	0.702675 (9)	150	200	0.513224 (45)	3	59								
88R4-110-113	443.07				0.513170 (40)	1	66	0.702941 (9)	15	259	0.513135 (16)	3	82		
90R3-22-27	451.85	0.702600 (8)	200	200	0.513175 (24)	2	93	0.703196 (36)	120	501	0.513179 (3)	30	203		
104R3-113-115	519.76	0.702660 (9)	200	200	0.513127 (46)	2	77	0.703000 (8)	30	240	0.513125 (12)	8	80		
117R3-86-87	581.70													0.702999 (8)	0.513170 (8)
125R2-119-121	614.06													0.702941 (9)	0.513171 (10)
149R2-16-21	733.49	0.702611 (26)	200	200	0.513213 (40)	5	95	0.702861 (13)	30	208	0.513180 (72)	15	125		
149R2-68-71a	734.00	0.703272 (10)	200	200	0.513096 (64)	2	55	0.703238 (10)	15	222	0.512986+ (41)	2	94		
149R2-68-71b	734.00							0.704235 (57)	27	110	0.513078 (77)	5	56		
153R1-25-24	751.25													0.702938 (8)	0.513186 (8)
175R2-25-28	853.00	0.702662 (25)	200	100	0.513214 (34)	1	132	0.703571 (14)	50	272	0.513121 (18)	5	98		
179R4-118-123	875.33													0.702644 (7)	0.513154 (9)
187R3-23-27	911.63	0.702611 (8)	200	200	0.513121 (34)	6	74	0.702893 (9)	40	224	0.513135 (23)	10	80		
205R4-63-66	990.38													0.702698 (8)	0.513190 (9)
214R1-138-143	1031.01							0.702961 (10)	25	201	0.513106 (10)	5	139		
227R1-112-117	1093.15	0.702575 (8)	250	200	0.513179 (36)	2	76	0.702963 (10)	25	219	0.513163 (23)	5	86		
227R2-28-33	1093.74	0.702732 (8)	200	189	0.513012 (33)	3	108	0.702959 (10)	35	203	0.513116 (10)	5	135		
229R1-66-71	1102.29	0.702566 (8)	200	180	0.513090 (30)	3	131	0.702744 (8)	40	200	0.513155 (10)	10	93		
242R2-35-39	1174.37	0.702488 (9)	200	240	0.513099 (44)	2	79	0.702941 (10)	50	333	0.513137 (12)	17	81		
249R1-54-56	1197.25	0.702564 (9)	200	200	0.513134 (30)	3	83	0.702719 (10)	60	200	0.513177 (16)	12	58		
250R1-83-87	1202.35				0.513019 (184)	1	40	0.702836 (9)	30	301	0.513157 (20)	7			
250R2-60-66	1203.59	0.702530 (9)	200	200	0.513236 (116)	3	84				0.513235 (22)	20	121		
251R1-60-65	1206.93	0.702569 (9)	150	181				0.703256 (60)	10	88	0.513172 (17)	4	136		
251R3-59-62	1209.77							0.704269 (18)	15	241	0.513179 (16)	5	136		
252R4-3-6a	1215.43	0.702612 (6)	170	340	0.513174 (33)	2	106	0.702920 (9)	30	208	0.513207+ (23)	5	84		
252R4-3-6b	1215.43	0.702633 (8)	200	192				0.703130 (16)	80	155	0.513230 (109)	16	45		
252R4-3-6c	1215.43							0.707908 (11)	49	134	0.512857 (18)	10	67		
253R1-40-41	1216.31													0.702618 (8)	0.513204 (9)
253R3-0-3	1218.63													0.702600 (10)	
253R3-45-78	1219.07							0.702927 (8)	15	222	0.513151 (15)	2	97		
257R1-95-100a	1236.08	0.702594 (9)	200	200	0.513048 (56)	3	64	0.702884 (9)	30	240	0.512800+ (15)	5	73		
257R1-95-100b	1236.08	0.702574 (15)	200	119	0.513088 (49)	6	75	0.707341 (11)	41	103	0.512927 (38)	11	68		
257R1-95-100c	1236.08							0.706109 (12)	82	193	0.513100 (16)	22	65		
257R1-95-100d	1236.08							0.703154 (50)	44	63	0.513192 (26)	12	55		

Table S1. *Continued*

Sample	depth (mbsf)	Plagioclase 87Sr/86Sr	Sr*	n	143Nd/144Nd	Nd*	n	Clinopyroxene 87Sr/86Sr	Sr*	n	143Nd/144Nd	Nd*	n	Whole rock 87Sr/86Sr	143Nd/144Nd
260R1-14-16	1249.65													0.702664 (7)	0.513205 (7)
268R2-78-81	1290.03	0.702574 (8)	300	200				0.702865 (12)	35	227	0.513175 (17)	10	100		
268R3-6-12	1290.69				0.513301 (104)	2	73	0.702937 (9)	30	380	0.513194 (12)	10	108		
287R1-6-8	1377.67													0.702779 (8)	0.513191 (9)
292R1-75-77	1397.56				0.513169 (136)	1	80	0.703858 (14)	40	227	0.513168 (30)	9	39		
1310-A1-0-13	0.07													0.702576 (9)	0.513214 (11)
1310-A1-13-19	0.16													0.702567 (10)	0.513210 (11)
1310-B1R1-0-5	0.03													0.702572 (8)	0.513203 (10)
1310-B1R1-62-69	0.66													0.702560 (9)	0.513207 (16)
1310-B1R1-139-143	1.41													0.702572 (9)	0.513198 (9)
1311-AR1-0-9	0.05													0.702515 (10)	0.513220 (11)
1311-AR1-48-54	0.51													0.702528 (8)	0.513223 (9)
1311-AR1-99-104	1.02													0.702525 (9)	0.513225 (11)
1311-AR1-136-142	1.39													0.702499 (5)	0.513226 (9)

2 SE (in parentheses) are given in terms of least unit cited: e.g., 0.702643 (8) represent 0.70264 ± 0.000008.

n: number of cycles for each analyses

* Amount of Sr and Nd (in ng) analysed calculated from Sr and Nd concentration and estimated volume of milled mineral

+ 143Nd/144Nd ratios uncorrected for Sm: 0.512936±31 for 149R2-68-71a, 0.513169±19 for 252-R4-3-6a and 0.512783±15 for 257R1-95-100a.